

Jie Zhang

Peng Cheng

Department of Mechanical Engineering,
Columbia University,
New York, NY 10027

Wenwu Zhang

Michael Graham

Global Research Center,
General Electric Company,
Niskayuna, NY 12309

Jerry Jones

Native American Technologies Company,
Golden, CO 80401

Marshall Jones

Global Research Center,
General Electric Company,
Niskayuna, NY 12309

Y. Lawrence Yao

Department of Mechanical Engineering,
Columbia University,
New York, NY 10027

Effects of Scanning Schemes on Laser Tube Bending

Four laser scanning schemes for tube bending, including point-source circumferential scanning, pulsed line-source axial procession, and line-source axial scanning without and with water cooling are investigated in numerical simulation. The coupled thermo-mechanical model established using the finite element method is validated and applied to predict the bending deformation and help better understand bending mechanisms under different schemes. The influence of important parameters such as beam coverage, scanning velocity and cooling offset on the deformation is investigated in detail. Parametric studies are carried out to determine proper processing windows at which the largest bending can be obtained. The deformation characteristics, including the wall thickness variation and the cross-section distortion produced by different scanning schemes are analyzed, along with the processing efficiency. [DOI: 10.1115/1.2113047]

1 Introduction

Tube bending has many applications especially in the automotive and aerospace industries. So far mechanical bending has been the primary technique used in industry. Mechanical tube bending has a limitation on the minimal bending radius due to material thinning at the extrados. Extrados is defined in this paper as the outside arc of the bent tube, and intrados is the inside arc of the bent tube. Pressure bending may be adopted to reduce material thinning at extrados. At the intrados, compressive stress may induce the buckling and wrinkling of the material. Mandrels can be used to prevent these forming defects. However, use of pressure bending and mandrels increases the complexity of mechanical bending facilities. In addition, mechanical tube-bending requires complex tooling for multiaxis bending. Hydroforming of tubular components has attracted significant interest in recent years but it requires hard tooling. As a spring-back-free and dieless technique, laser forming accomplishes the forming task by intensively and locally heating the workpiece and thus inducing thermal deformation. In laser tube bending, material thinning at the extrados is nearly absent. With the flexible delivery of laser beam, multiaxis tube bending can be readily realized.

Laser tube bending is normally done via a point laser source scanning along tube circumference, as shown in Fig. 1(a). Silve et al. [1] investigated the effects of different scanning sequences on bent tube profile. Kraus [2] analyzed the temporal development of

plastic straining and restraining in the laser bending of square cross-section tubes with finite element analysis. It was found that plastic restrain primarily occurs in the cooling-off phase. Li and Yao [3] studied the laser bending mechanism of circular cross-section tubes of mild steel. The deformation characteristics such as wall thickness variation, ovality, and protruded intrados were compared with those of mechanical bending. However, the circumferential scanning scheme with a point laser source achieves a very small bending angle per scan, and thus requires multiple scans at the same location or at different axial positions in order to obtain practical bending angles.

The advent of high power direct diode lasers offers a rectangular laser beam shape, among other advantages. The rectangular beam shape is well suited for surface processing. Bachmann [4] described how direct diode lasers were applied in surface hardening, cladding and soldering. The application of direct diode lasers into laser forming of plates has also been investigated. Lawrence [5] conducted a comparative investigation of the efficiency of CO₂ laser and diode laser in the forming of mild steel sheets. Lopez et al. [6] applied a diode laser in the forming of stainless steel, AlMg3 and St 14 sheets and investigated the correlation between bending angle and parameters such as path feed rate, number of irradiations, sheet materials, and sheet thickness.

The technique of beam shaping can be used to transform a circular beam into noncircular shapes. Shealy [7] presented an overview of the development and applications of the various geometrical methods for laser beam shaping. The influence of different beam shape on the processing results has been studied by several scientists. Mucha et al. [8] studied the effects of circular and rectangular beam on the deformation of plates. Triantafyllidis

Contributed by the Manufacturing Engineering Division of ASME for publication in the JOURNAL OF MANUFACTURING SCIENCE AND ENGINEERING. Manuscript received August 11, 2004; final manuscript received June 11, 2005. Review conducted by K. Rajurkar.

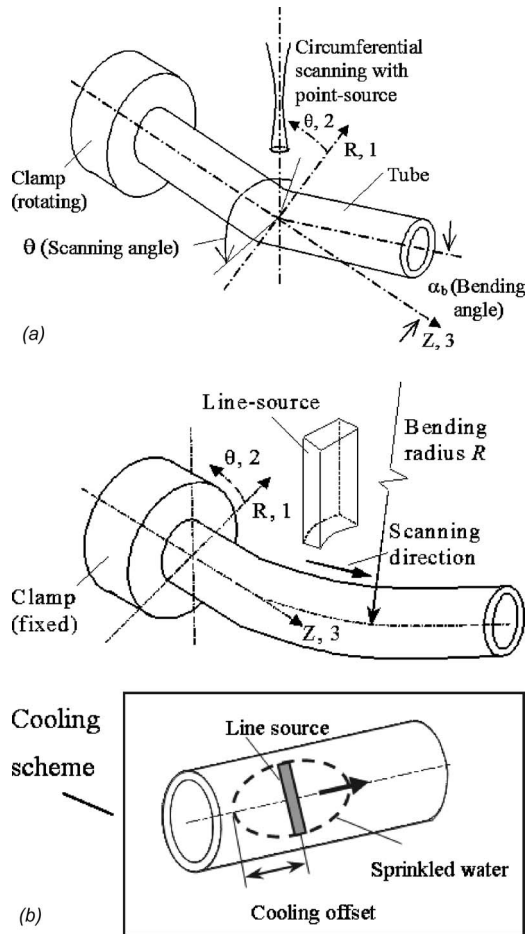


Fig. 1 Schematic of scanning schemes. (a) Circumferential scanning by a point laser source. (b) Axial scanning by a line laser source and cooling scheme.

et al. [9] studied the effect of various beam shapes on the quality of ceramics after laser surface treatment with the criterion of avoiding crack formation.

The availability of a laser beam with a rectangular shape opens up the possibility of axial scanning in laser tube bending. Compared to circumferential scanning scheme which need multiple passes and is too time consuming, the axial scanning of a rectangular (or line) source can potentially generate sufficient bending in a single axial scan. It is important to understand the process. It is the aim of this paper to numerically study the bending mechanism, bending characteristics, and suitable operating conditions of various schemes of axial scanning by a line source, and to compare this with circumferential scanning by a circular (or point) source.

2 Scanning Schemes

Continuous point-source circumferential scanning (referred to as scheme I) refers to a circular beam irradiating along the tube circumferential direction through a prescribed scanning angle, as shown in Fig. 1(a). Multiple scans either at the same location or different axial locations are usually required to generate sufficient bending. In this paper, the inclusion of scheme I is for the purpose of validating the numerical model established in the present paper with existing experimental results, and comparatively studying it with different axial scanning schemes. More details about this scanning scheme can be found in Ref. [3].

Scanning scheme II involves a pulsed line-source procession along the tube axis. Inclusion of this scheme is primarily for gain-

Table 1 Four tube scanning schemes

No.	Scheme	Beam shape	Scanning direction
I	Continuous point-source circumferential scanning	Circular	Circumferential
II	Pulsed line-source axial procession	Rectangular	Axial procession
III	Continuous line-source axial scanning	Rectangular	Axial
IV	Continuous line-source axial scanning with water cooling	Rectangular	Axial

ing a preliminary understanding of axial scanning and leads to the following two scanning schemes (scanning schemes III and IV). Continuous line-source axial scanning is shown in Fig. 1(b) and is referred to as scanning scheme III. Under this scheme, a multiple-scan achieved bending angle under scheme I can be produced by the single axial scan. Hence, the bending efficiency will be enhanced. The tube bending increases with the axial mechanical constraint exerted by unheated material on the currently heated material. To avoid the decrease of axial mechanical constraint due to scanning-caused heat accumulation, it is necessary to remove the amassed heat within proper time by forced cooling. So scheme IV, continuous line-source axial scanning with water cooling, is also investigated. The four scanning schemes are summarized in Table 1.

2.1 Laser Sources and Tube Parameters. In the simulation of point-source scanning, the laser system is considered to be CO₂ laser with a maximum output power of 1500 W and a power density that follows a Gaussian distribution. In the simulation of line-source scanning, the laser system is considered to be a diode laser with a maximum output power of 4000 W. The high power diode laser has a rectangular beam shape 1–6 mm in width and 3–20 mm in length. The energy intensity has a Gaussian distribution in the width direction and a top-hat distribution in the length direction. The rectangular beam is projected evenly on the part of tube circumference through the beam shaping technique. In the simulation, the beam length is transferred into the beam coverage. *Beam coverage*, which centers vertically, is defined as the laser-irradiated range along the tube circumference. Under all schemes, it is supposed that the tube is coated with graphite to enhance the absorption of laser power. The material of the tube is low carbon steel, AISI1010. The absorption coefficient of graphite-coated AISI1010 is assumed to be 0.6. The outside diameter of the tube is 12.7 mm, the wall thickness of the tube is 0.89 mm, and the tube length is 100 mm. Under schemes II and III, a tube length of 50 mm is also modeled to reduce the computational time of finite element method (FEM). The tube length of 600 mm is also simulated to validate the feasibility of scheme IV in long-tube bending. The simulated processing conditions are listed in Table 2.

2.2 Cooling Arrangement. Due to the higher heat-transfer coefficient, water cooling is applied in the axial scanning instead of air cooling. Thus, the massive amassed heat can be removed quickly and effectively, which is very important for the generation of axial mechanical constraint. An elliptical water sprinkler is as-

Table 2 Processing conditions. *d* is the diameter of the circular beam; *w* is the width of the rectangular beam.

Scheme	Power (W)	Velocity (mm/s)	Beam size (mm)	Beam coverage of tube
I	780	1.57 (rad/s)	$d=11$	180° (scanning angle)
II	200–800	1–6	$w=1-6$	30°–180°
III	200–600	4–50	$w=4$	120°
	1350–2000			
IV	425 and 1550	4 and 20	$w=4$	120°

sumed to be coaxial with the laser beam to move with the laser in synchronization, as shown in Fig. 1(b). Water is sprinkled only along the elliptical edge of the sprinkler and other parts of the sprinkler are sealed. The major axis of the sprinkler is coincident with the tube axis and its length can be adjusted to suit different scanning speeds. The minor axis has the length covering the optimal beam coverage. The half length of the major axis of the sprinkler is defined as *cooling offset*.

It is assumed that water flows out of the sprinkler under gravity and covers the entire tube surface except the elliptical area where the laser irradiates. The heat-transfer coefficient of water on the tube can be evaluated with the model of a tube in a crossflow [10]. The Nusselt number is calculated as

$$N_{ud} = 0.3 + \frac{0.62R_e^{1/2}P_r^{1/3}}{[1 + (0.4/P_r)^{3/2}]^{1/4}} \left[1 + \left(\frac{R_e}{282,000} \right)^{5/8} \right]^{4/5} \quad (1)$$

where P_r is Prandtl number, P_{ed} is Peclet number defined as $P_{ed} = R_e P_r$, which is valid for the range of $10^2 < R_e < 10^7$ and $P_{ed} > 0.2$. Thus, the heat-transfer coefficient is defined by

$$h = N_{ud} \left(\frac{k}{D} \right) \quad (2)$$

where k is the thermal conductivity and D is the outer diameter of the tube.

3 Numerical Simulation

The following assumptions have been made in the numerical simulation. The tube material is isotropic and has constant density. Material properties such as the modulus of elasticity, heat transfer properties, thermal conductivity, specific heat and flow stress are temperature dependent, and the flow stress is also strain and strain rate dependent. Heat generated by plastic deformation is negligible compared with intensive heat input from the laser beam. No melting and no external forces are involved in laser bending.

Laser tube bending is numerically simulated as a sequentially coupled thermal-mechanical process [11]. In the thermal analysis, the temperature distribution of the tube can be described by

$$\rho c_p \frac{\partial T}{\partial t} = \nabla \cdot (k \nabla T) \quad (3)$$

where ρ is the density and c_p is the specific heat. The associated boundary condition of the heat conduction equation is $AF_l \cdot \hat{n} =$

$-\hat{n} \cdot (k \nabla T)$ at $r = D/2$, where A is the absorption coefficient of material, F_l is the heat flux of laser beam, and \hat{n} is the unit vector normal to the surface pointing to the tube. All the surfaces are subject to heat convection $q = h(T - T_0)$, where h is the convective heat-transfer coefficient, T is the surface temperature and T_0 is the ambient temperature. The heat radiation is $q = \varepsilon \sigma (T^4 - T_0^4)$, where ε and σ are emissivity and Stephan-Boltzmann constant, respectively.

Without the consideration of body forces, the following equation of equilibrium is satisfied due to no external forces acting on the tube

$$\frac{\partial \sigma_{ij}}{\partial x_j} = 0 \quad (4)$$

The mean strain rate is written as

$$\dot{\varepsilon}_{kk} = \frac{1 - 2\nu}{3E} \dot{\sigma}_{kk} + \alpha \dot{T} \quad (5)$$

where E is Young's modulus, ν is Poisson's ratio, $\dot{\sigma}_{kk}$ is the mean stress, and α is the thermal expansion coefficient. The deviatoric strain, e_{ij} , including elastic strain, e_{ij}^e , viscoelastic strain, e_{ij}^v , and plastic strain, e_{ij}^p , is written as

$$\dot{e}_{ij} = \dot{e}_{ij}^e + \dot{e}_{ij}^v + \dot{e}_{ij}^p \quad (6)$$

where $\dot{e}_{ij}^e = (1/2G)\dot{s}_{ij}$ and $\dot{e}_{ij}^v = (1/2\eta)s_{ij}$, where G is the shear modulus, η is the viscosity constant, and s_{ij} is the principal component of the deviatoric stress tensor. When Von Mises criterion $\sqrt{3/2}(\sigma_{ij}\sigma'_{ij}) = Y$ is used as the yield criterion, the plastic strain follows the flow rule, that is

$$e_{ij}^p = 0 \text{ if } \frac{1}{2}s_{ij} \leq Y^2(T), \text{ or if } \frac{1}{2}s_{ij} = Y^2(T) \text{ and } s_{ij}\dot{s}_{ij} - 2YY'\dot{T} \leq 0 \quad (7)$$

$$e_{ij}^p = \dot{\lambda}s_{ij} \text{ if } \frac{1}{2}s_{ij} = Y^2(T) \text{ and } s_{ij}\dot{s}_{ij} - 2YY'\dot{T} \geq 0 \quad (8)$$

where $\dot{s}_{ij}^v = 2G(\dot{e}_{ij} - \dot{e}_{ij}^v)$, and $Y(T)$ is the Von Mises yield stress as a function of temperature. Therefore, the combined stress-strain relations can be expressed as [12]

$$\dot{\varepsilon}_{ij} = s_{ij}\dot{\lambda} + \frac{1}{2G}\dot{s}_{ij} + \delta_{ij}\left(\frac{1 - 2\nu}{3E}\right)\dot{\sigma} + \delta_{ij}\alpha\dot{T} \quad (9)$$

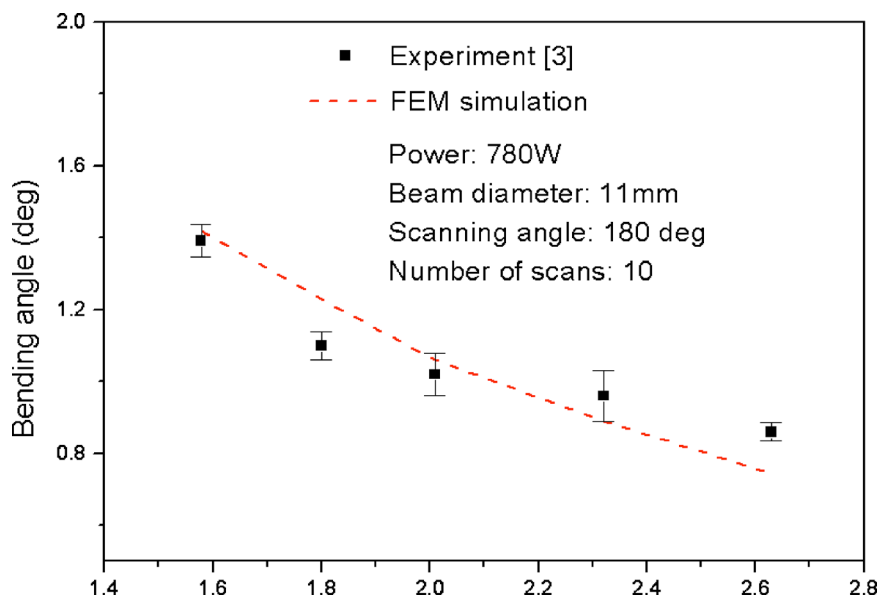


Fig. 2 FEM simulation validation with experimental results (scheme I)

Due to the characteristics of laser tube bending, nonlinear analysis is used in the model of finite element analysis (FEA). A commercial FEA software *ABAQUS* is used. The same mesh is created for both heat transfer and structural analysis. In structural analysis, using elements of C3D20 without shear locking and hourglass effect is suitable for a bending-deformation-dominated process such as laser forming. To remain compatible with the structural analysis, three-dimensional heat transfer elements of DC3D20 are used for the heat transfer analysis. A user-defined subroutine is developed in *FORTAN* to describe the heat flux from the laser beam. All the points in the plane at $z=0$ shown in Fig. 1, which is the scanning plane (plane of symmetry) under scheme I and the end-surface close to the start of the scanning path under schemes II, III, and IV, are fixed in the axial direction. In this plane, two adjacent points at the bottom of the tube are also fixed

in the radial and tangent directions to eliminate the rigid body motion.

4 Results and Discussions

4.1 Continuous Point-Source Circumferential Scanning.

To validate the FEM model of tube bending established in the present paper, scheme I is first considered. Figure 2 shows the comparison of bending angle simulated in the present paper and the existing experimental results [3]. It is seen that the simulated results agree with the experimental results. Therefore, the numerical model is capable of simulating laser tube bending.

Under scheme I, the temperature gradient in the tube thickness direction within the heat affected zone is small due to the large beam size used. The condition induces upsetting and subsequent

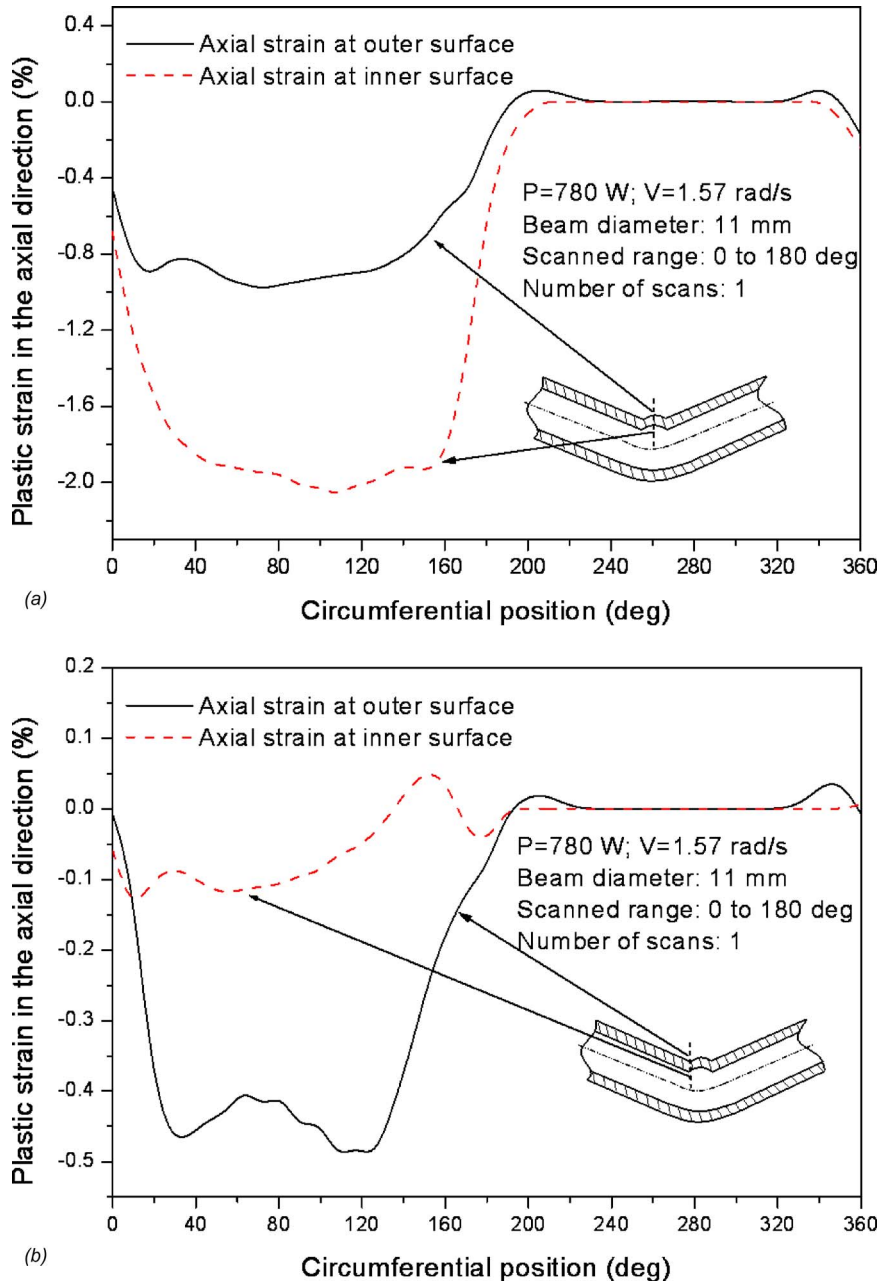


Fig. 3 Distribution of axial plastic strain along the circumferential position under scheme I, the point-source circumferential scanning scheme (a) at the center of heat affected zone; and (b) at the location slightly off the center of heat affected zone

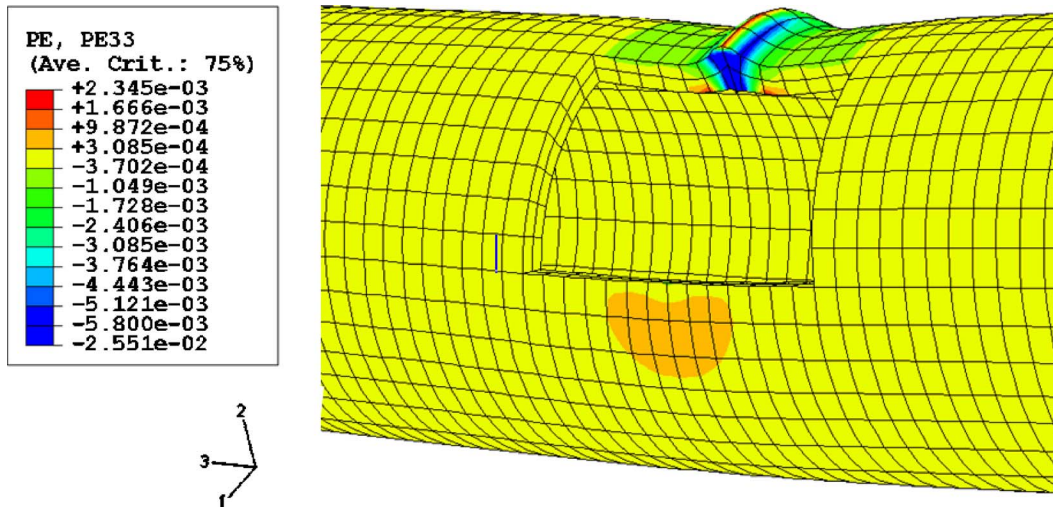


Fig. 4 Cutoff schematic of bent tube with axial plastic strain (PE33) along the intrados under scheme II, the pulsed line-source axial procession scheme (deformation $\times 50$, irradiating time: 1 s, beam width: 4 mm, energy intensity: 8 J/mm^2 , outer diameter of tube: 12.7 mm, tube thickness: 0.89 mm)

bending [13]. Another known phenomenon is a protrusion at the intrados under scheme I [3]. Figure 3 shows the distribution of axial plastic strain along two different circumferential cross sections produced by one scan pass. It is seen that the axial plastic strain at the outer surface is smaller than that at the inner surface in the center of heat affected zone, while the trend reverses at the location slightly off the center of heat affected zone. This causes the protrusion in the intrados. Therefore, the distribution of the axial plastic strain at the latter location can more clearly reflect the tube bending dominated by the upsetting mechanism. This is the reason that the axial plastic strain at this location is used to analyze the bending process in the following sections.

4.2 Pulsed Line-Source Axial Procession

4.2.1 Mechanism of Pulsed Line-Source Axial Procession. Under scheme II, the tube is irradiated in an axial procession of a pulsed line source, which is simplified as a series of stationary pulses sequentially applied at different axial locations. In the simulation, these pulses are assumed to be independent of each other without considering the pulse repetition rate. Pulse width is 1 s, and the time spacing between two pulses is 300 s. Figure 4 shows the cutoff schematic of tube bent by one of these pulses at a particular location to investigate the net deformation induced by one pulse to better understand this scanning scheme. The pulsed beam is 4 mm in width and is assumed to radially irradiate part of tube surface (120°). As a result, a strip of tube material is heated simultaneously. The extent of the beam irradiated area is large compared to the tube thickness. The deformation shown in Fig. 4 indicates a distribution of the axial plastic strain along the intrados similar to that under scheme I (Fig. 3). One protrusion at the intrados can be seen in Fig. 4. It is clear that the pulsed line-source axial procession under the processing condition used bends tube through the upsetting mechanism.

4.2.2 Effect of Beam Coverage. In Ref. [3], it was found that the scanning angle (equivalent to beam coverage) of 270° was probably the optimal one under scheme I. Under the pulsed line-source axial procession scheme, beam coverage influences the tube bending more significantly because bending through the simultaneous heating of a strip of tube material makes more important the mechanical constraint in the circumferential direction, which depends on the beam coverage. Due to the geometrical characteristics of a line source, the beam coverage is restricted to the range below 180° .

Figure 5 shows the change of bending angle with the beam

coverage under the same laser intensity. It is seen that the bending deformation increases with the beam coverage to a maximum value, before it drops. In order to eliminate the effect of energy intensity, the laser power is adjusted to keep the constant energy intensity of 8 J/mm^2 for different beam coverage values. Figure 6 shows the time history of temperature at the point on the intrados irradiated by the beam center with two beam coverage values (120° and 180°). It is observed that they almost experience an identical thermal cycle. Heated material is thermally expanded to the same extent in each case. Therefore, the variation of bending angle with the beam coverage comes from the difference in the mechanical constraint.

Figure 7 presents the distribution of axial and circumferential plastic strain at the outer surface along the intrados with the beam coverage of 120° and 180° . There is the similar pattern of the plastic strain distribution at the inner surface. Confined with the paper space, the latter is not presented. It can be seen that at each location the magnitudes of plastic strain in axial and circumferential directions are almost the same while the direction (tensile or compressive) is opposite, so that the variation of tube thickness can be neglected if assuming volume constancy. Therefore, the discrepancy in the axial and circumferential plastic strain distribution does not result from the variation of the tube thickness during the bending, but from the different beam coverage. In the case of 180° , the axial plastic strain remains tensile and the circumferential plastic strain remains compressive. This is due to the fact that the mechanical constraint in the axial direction decreases as a result of simultaneous 180° circumferential heating. The tensile strain in the axial direction causes the circumferential strain to be compressive in order to maintain volume constancy. As a result, the bending angle diminishes under 180° beam coverage because compressive axial strain is primarily responsible for bending. In the case of 120° beam coverage, it is better to examine a location slightly off the beam center because of the reason stated earlier under scheme I. It is seen that the axial plastic strain is compressive and the circumferential strain is tensile. This is because the 120° beam coverage better preserves the mechanical constraint in the axial direction and thus a larger bending angle results.

To illustrate the point more closely, Fig. 8 shows the time history of axial and circumferential plastic strain at the outer surface slightly off the beam center. For the case of 120° beam coverage, the axial strain is momentarily tensile before it quickly becomes

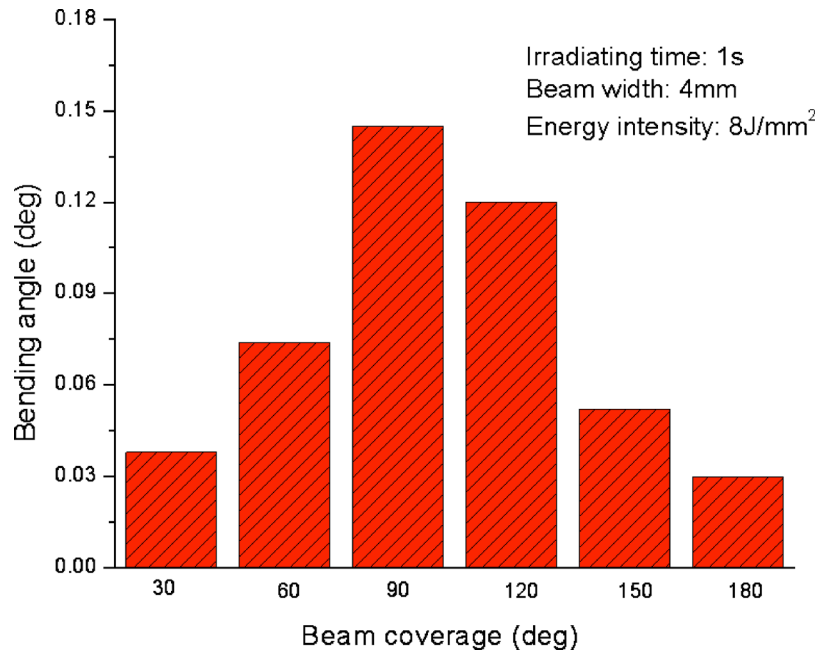


Fig. 5 Relationship of beam coverage with bending angle under scheme II, the pulsed line-source axial procession scheme

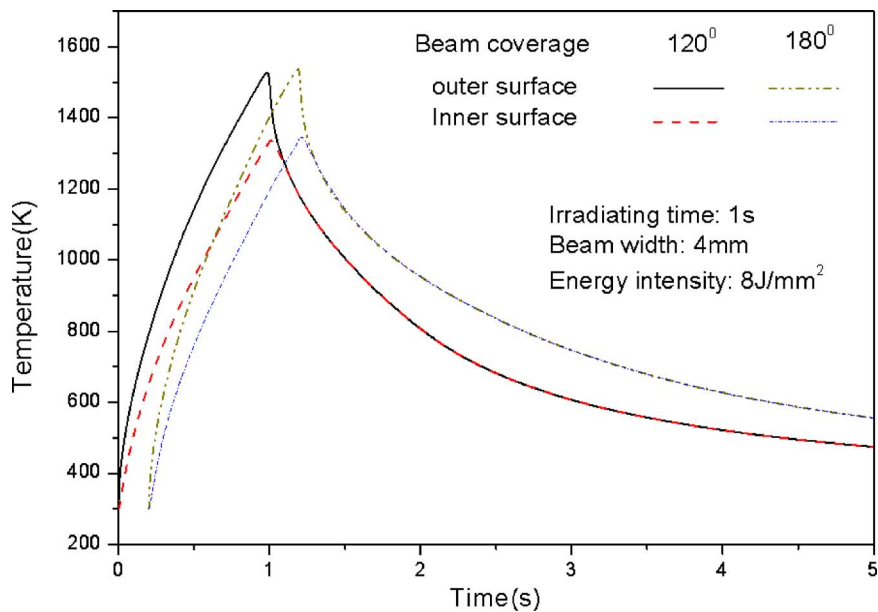


Fig. 6 Simulated time history of temperature with different beam coverage values under scheme II (0.2 s time delay between two cases for viewing clarity)

deeply compressive due to the larger restriction from the surrounding material. As a result, a much larger bending angle is obtained.

4.2.3 Parametrical Study. Design Experiments [14] (DOE) is applied in the search of better processing parameters for scheme II. Considering the processing parameters for circumferential scanning, the limits of available diode lasers, and the requirement of no melting, the initial value of the DOE is set for laser power (x_1) as 300 and 700 W, irradiating time (x_2) as 0.5 and 1.5 s, and beam width (x_3) as 3 and 6 mm. The beam coverage is set as constant of 120°. The DOE experiments are carried out via FEM simulation. The response is bending angle and is described by a first-order model $\hat{y}=b_0+bx^T$, where \hat{y} and $x=[x_1,x_2,x_3]^T$ are esti-

mated response and decision variable vector, respectively, $b=[b_0,b_1,b_2,b_3]$ are coefficients determined using the least square regression. A series of responses in the steepest ascent direction are calculated and compared with the corresponding simulation results to adjust the steepest ascent direction. Through five adjustments, the final first-order model is obtained as $\hat{y}=0.166+0.421x_1+0.306x_2-0.085x_3$. This model reflects that the bending angle increases with laser power and irradiating time, and decreases with the beam width. For the tube with the specification mentioned before, the optimal processing parameters are determined as laser power of 425 W, irradiating time of 1 s and beam width of 4 mm under this pulsed line-source axial procession scheme.

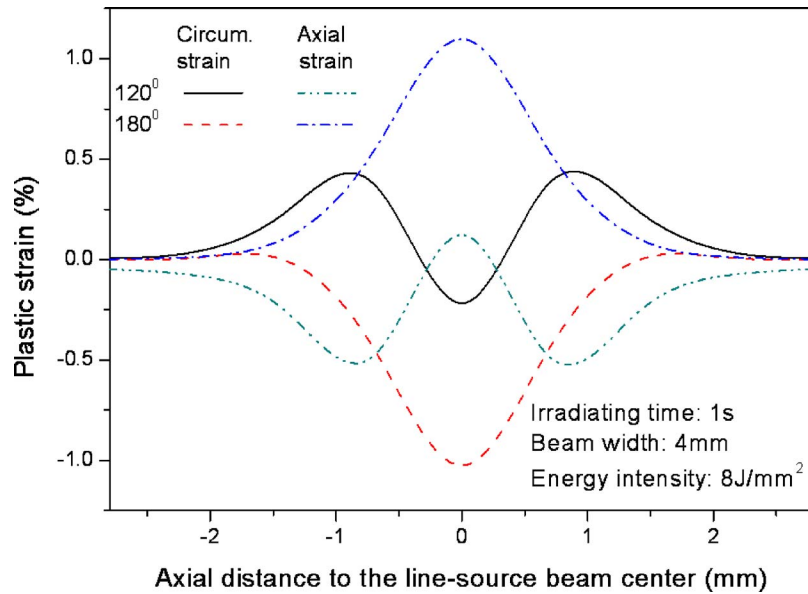


Fig. 7 Distribution of the circumferential- and axial-plastic strain at outer surface along the intrados, under scheme II, the pulsed line-source axial procession scheme

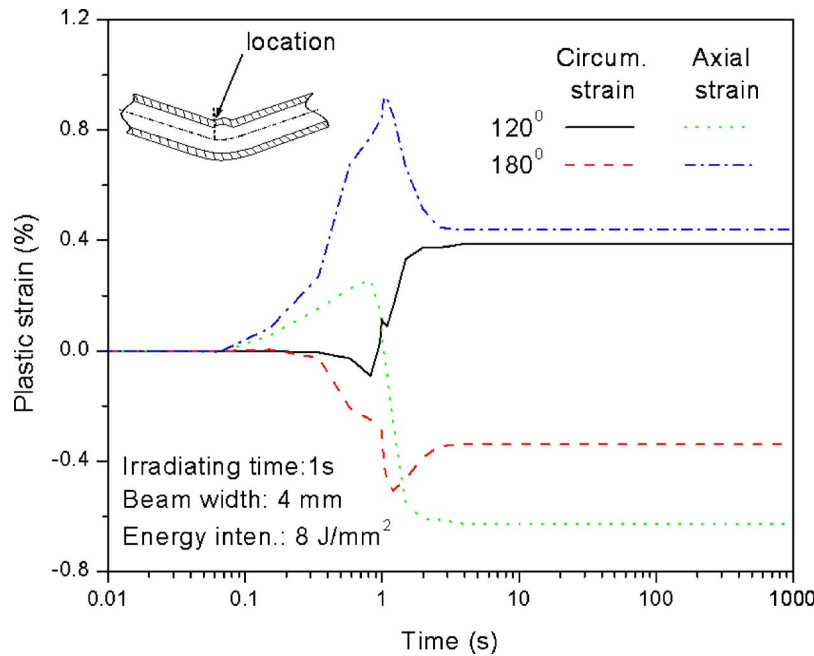


Fig. 8 Time history of circumferential- and axial-plastic strain of outer surface at the location slightly off the line-source center under scheme II, the pulsed line-source axial procession scheme

4.3 Continuous Line-Source Axial Scanning

4.3.1 Mechanism of Continuous Line-Source Axial Scanning. Continuous line-source axial scanning (scheme III) can be viewed as a series of rectangular pulses packed very closely irradiating a tube successively at a high frequency. As the moving beam reaches a particular location, the heated material there tends to expand thermally. Although the mechanical constraint from the scanned material preceding this location decreases to some extent due to the residual heat, the material in other directions can still confine the currently heated material from freely thermal expanding. As a result, compressive plastic strain occurs in the heated material and tube bends during the cooling phase. Figure 9 shows

the cutoff schematic of a bent tube scanned under scheme III and it also shows the axial plastic strain distribution, which is mostly compressive at the outer surface and inner surface along the intrados. This is the typical distribution of the axial plastic strain of the tube bent through the upsetting mechanism. It can be concluded that scheme III is still dominated by the upsetting mechanism.

In continuous line-source axial scanning, the bending of tube is better described by bending radius instead of bending angle, assuming the radius is largely constant for a particular bend. The geometrical relationship of central angle, radius, and arc length is applied in the conversion of bending angle and bending radius.

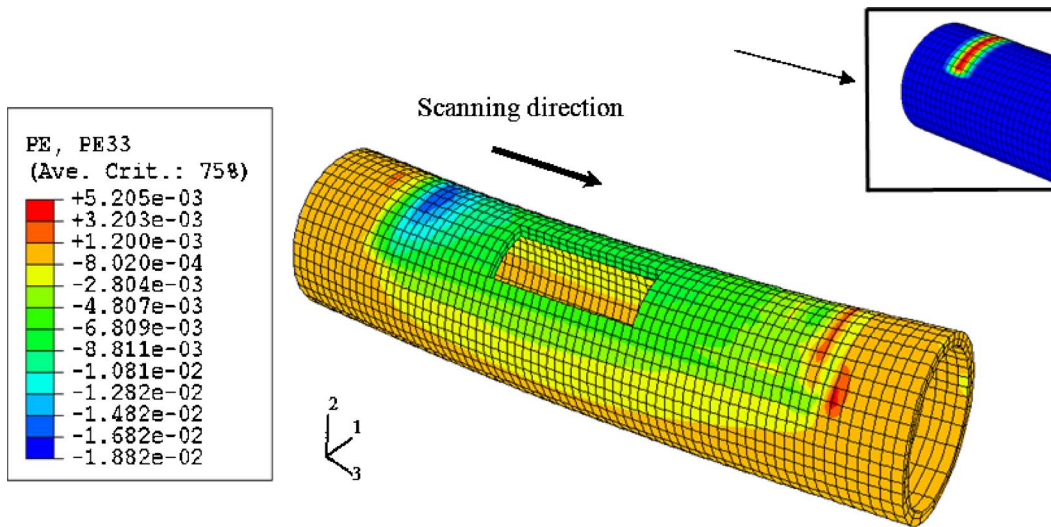


Fig. 9 Cutoff schematic of bent tube with typical FEM contour of axial plastic strain (PE33) under scheme III, the line-source axial scanning scheme (deformation $\times 5$, laser power: 1550 W, scanning velocity: 20 mm/s, beam width: 4 mm)

4.3.2 Parametric Study. The processing parameters under scheme III are investigated. The optimal processing parameters under scheme II may not be applicable here since a continuous moving heating source is involved. It is assumed that scanning velocity plays a key role in the deformation of tube under this scheme. Thus, a constant peak temperature approach [15] is used to specify power and velocity levels that produce about the same peak temperature. Figure 10 shows the variation of bending radius with these velocity levels. It can be seen that the bending radius decreases first then increases when the scanning velocity increases, and the minimum bending radius is generated at the velocity around 20 mm/s. Two cases are selected for analysis.

A typical temperature distribution along the tube intrados at the time when the beam center reaches the same point at two different velocity values is shown in Fig. 11. At the high velocity of 20 mm/s, the heat dissipation is smaller than that at the low

velocity so that the temperature difference between scanned material and cold material is steeper. Therefore, the cold material can apply larger constraint on the scanned material, which helps to increase the compressive strain. Moreover, more material at high temperature is also helpful to increase the final deformation. At the low velocity of 4 mm/s, the temperature tends to increase evenly in the scanned area, which is disadvantageous for cold material to restrict the thermal expansion. The distribution of axial plastic strain along the intrados at two different velocity values is plotted in Fig. 12. The pattern that the axial plastic strain under higher speed (20 mm/s) is larger than that under lower speed (4 mm/s) with the almost identical peak temperature on the scanned surface observed in Fig. 11 is in good agreement with the above analysis.

It is also shown in Fig. 11 that the temperature gradient

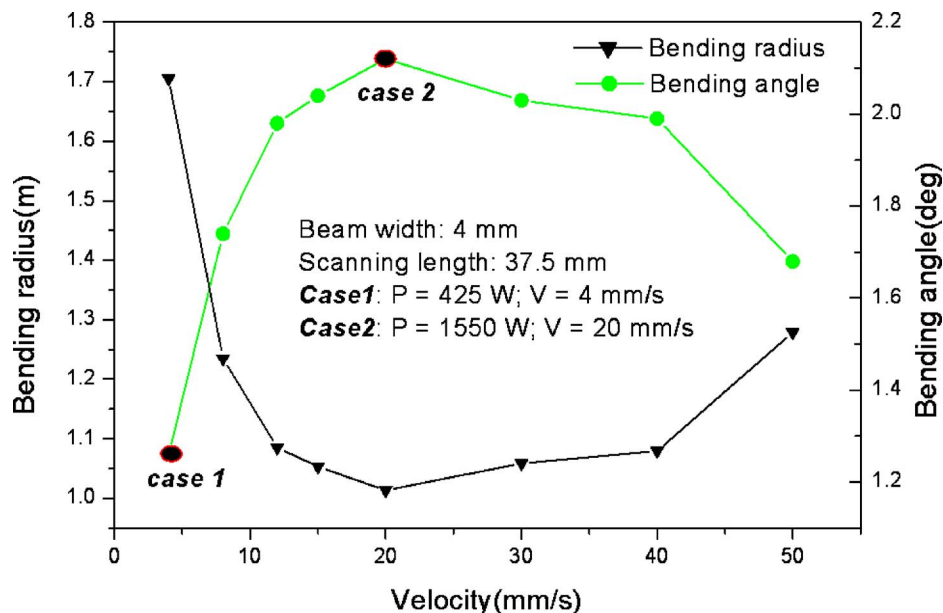


Fig. 10 Variation of bending radius with velocity under a constant peak temperature approach under scheme III, the line-source axial scanning scheme

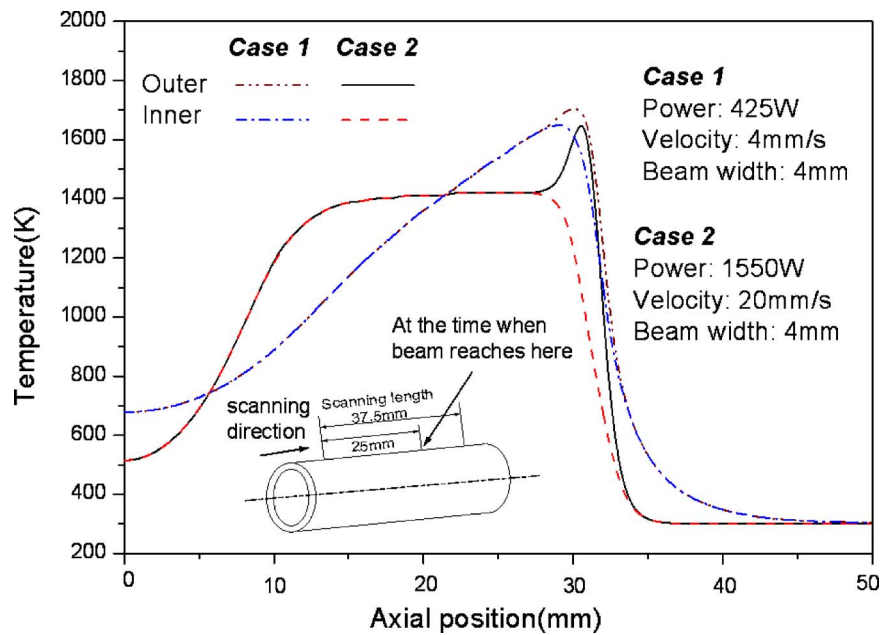


Fig. 11 Comparison of temperature distribution along the intrados when the line-source center reaches a typical position of the tube under scheme III, the line-source axial scanning scheme

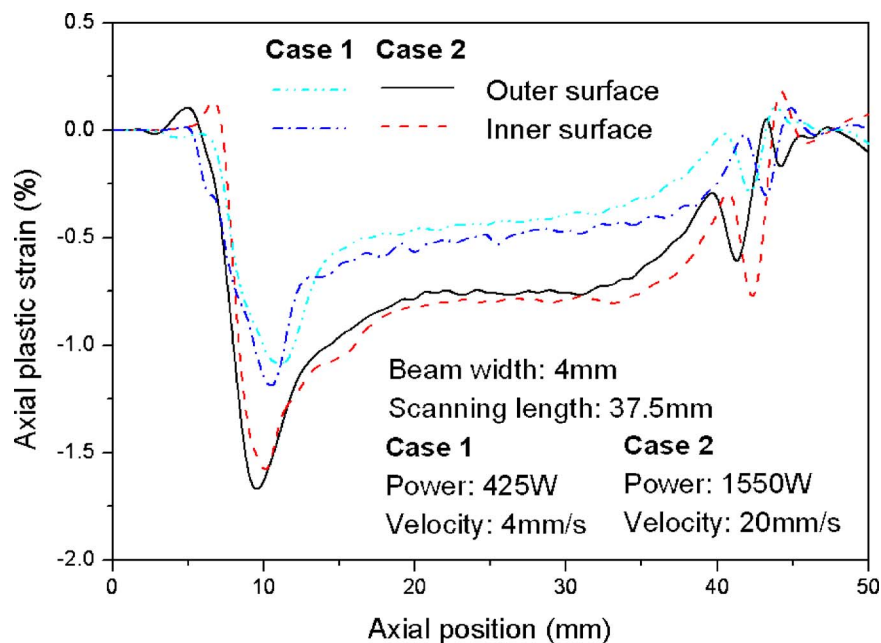


Fig. 12 Distribution of axial plastic strain along the intrados at different velocity values under scheme III, the line-source axial scanning scheme

between the outer and inner surfaces increases with the velocity. Within a certain range of velocity values, the discrepancy in strain between the outer and inner surfaces due to the temperature gradient is not large enough to change the mechanism of tube bending. However, if velocity continues increasing, the temperature gradient mechanism becomes more dominant in the deformation of the upper half tube. Only the outer surface has a large strain, and the inner surface with small or no strain assists the cold lower half tube to impede the tube in bending toward the laser beam. As a result, the bending deformation reduces and the bending radius goes up, which is presented in Fig. 10.

4.4 Line-Source Axial Scanning With Water Cooling

4.4.1 Effect of Water Cooling on Deformation of Tube. Figure 13 compares the temperature distribution on the irradiated surface when the tube is irradiated by a continuous line source with and without cooling given all other processing parameters the same. It is obvious that the extent of the heat affected zone behind the laser beam can be controlled effectively by the quick removal of heat under scheme IV. Figure 14 shows that the time history of axial plastic strain at the center of intrados under schemes III and IV, respectively. The compressive axial plastic strain obtained with

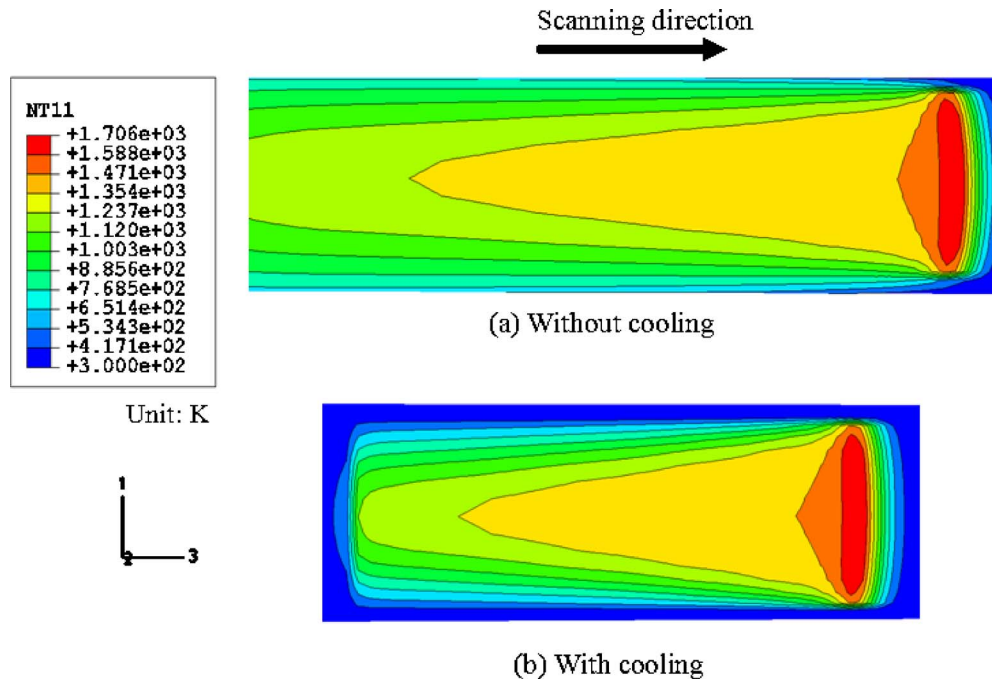


Fig. 13 Comparison of temperature distributions (NT11) under the line-source axial scanning without and with cooling schemes (schemes III and IV) (laser power: 1550 W, scanning velocity: 20 mm/s, beam width: 4 mm, cooling offset: 50 mm)

water cooling is much larger than that of without cooling, which shows that water cooling is helpful to increase the constraint to the heat affected zone especially in the region right behind the current location of the laser beam. Another interesting phenomenon is that the axial plastic strain at the outer and inner surfaces is both compressive which indicates that the upsetting mechanism is more active under schemes III and IV.

4.4.2 Relationship between Bending Radius and Cooling Offset. As discussed in Sec. 4.2.2, the sufficient circumferential constraint is necessary for the axial plastic strain to occur. This is

the reason that the elliptical sprinkler is utilized to also enhance the circumferential constraint. It is known that the axial constraint plays a more important role in the generation of the axial plastic strain. Whether water cooling positively affects the constraint in the axial direction or not is dependent on the cooling offset (defined in Fig. 1(b)). The effects of cooling offset on bending radius under two sets of processing parameters are presented in Fig. 15. The variation tendency of bending radius with the cooling offset is similar in two cases. The temperature history of the outer surface at the center of intrados with different cooling offsets and without

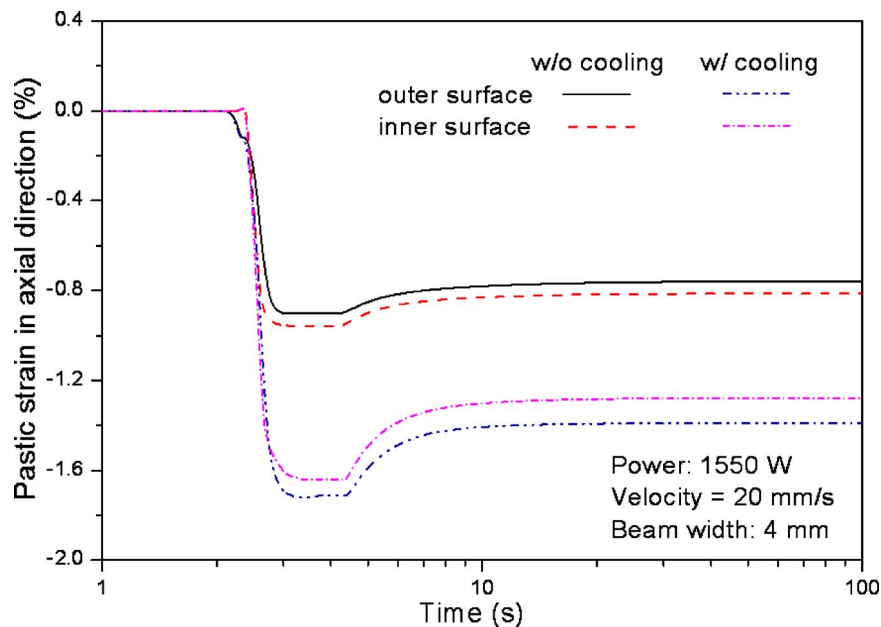


Fig. 14 Comparison of the time history of axial plastic strain at the center of intrados under the condition of the line-source axial scanning w/cooling and w/o cooling

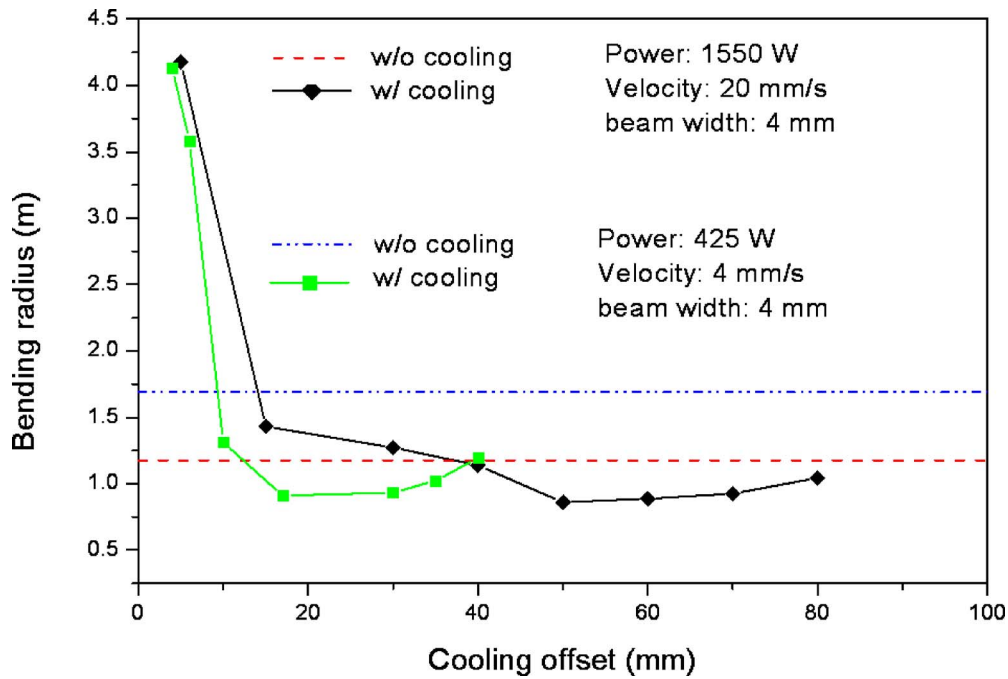


Fig. 15 Variation of the bending radius with cooling offset (which is defined as the half length at major axis of water sprinkler, see Fig. 1(b))

cooling is shown in Fig. 16. It is seen that the heat dissipates much faster with water cooling than without cooling. However, if the heated material is cooled too early by the sprinkler with a short offset ($l=30$ mm), it does not have enough time to obtain the maximal constraint from the cold surrounding material. The sprinkler with a longer cooling offset can augment plastic strain in two aspects: one is to increase the temperature gradient between heated and cold material; the other is to keep a longer heated length which is necessary to produce large deformation. Too long an offset will lead to failure of the water sprinkler in the genera-

tion of more axial mechanical constraint.

It is also seen in Fig. 15 that the optimal cooling offset at the lower velocity is smaller than that at the higher velocity. The reason is clear in that the scanned region at higher temperature is shorter due to the higher heat dissipation at the lower velocity. It is seen that the bending radius with cooling at the low velocity is reduced much more than that at the high velocity. Thus, it is proven again that the low velocity without cooling is not effective for continuous line-source scanning because higher heat dissipation leads to the reduced mechanical constraint in the axial

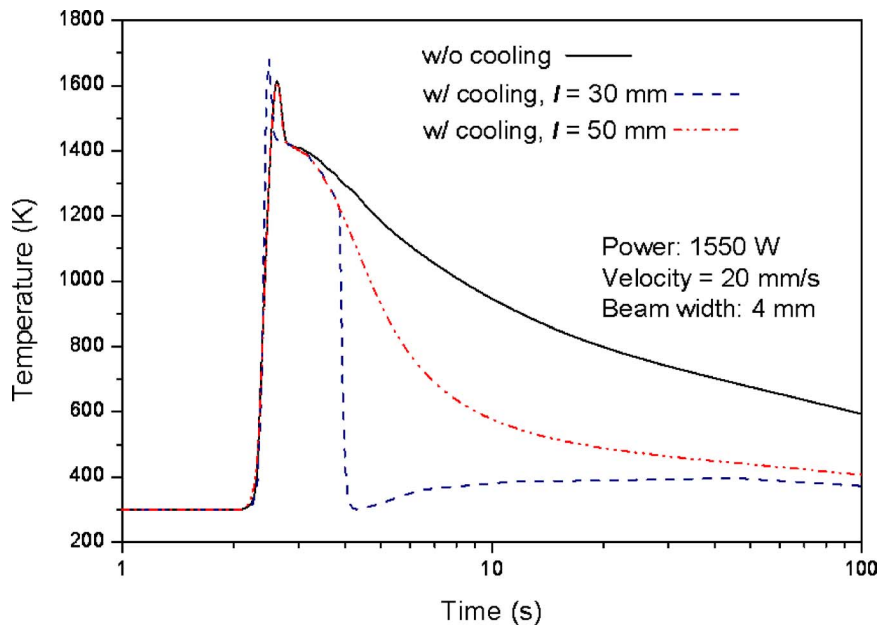


Fig. 16 Simulated temperature history of the outer surface at the center of intrados under different cooling offsets l

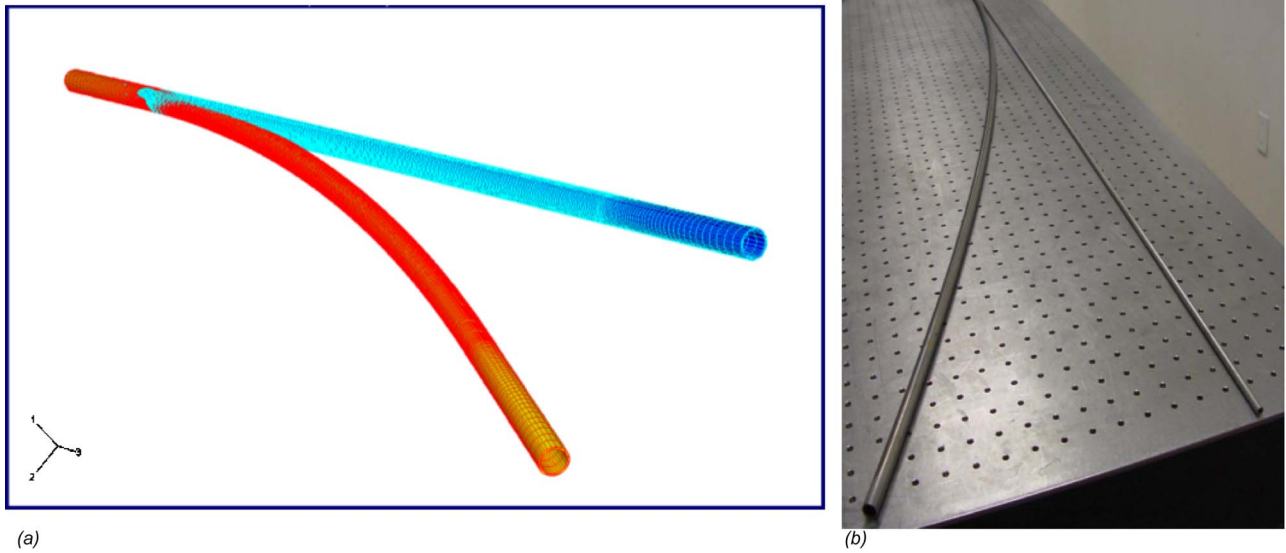


Fig. 17 Simulated and experimental results using line-source axial scanning with water cooling for tube outer diameter: 12.7 mm, wall thickness: 0.89 mm, and tube length: (a) 600 mm, with the FEM contour of axial plastic strain (PE33) and (b) 1800 mm

direction.

Under scheme IV, simulation of a tube of 600 mm in length is carried out as shown in Fig. 17(a). Preliminary experiments are carried out for tubes of 1800 mm in length with the same diameter and wall thickness (Fig. 17(b)). The simulation investigation reported in this paper lays the groundwork to suggest further experiments.

4.5 Comparison of Scanning Schemes. To eliminate the effect of tube length on deformation, tubes of 100 mm in length are simulated in the following comparison of four scanning schemes. Under scheme I, eight scans are sequentially applied with equal spacing in the axial direction. With the beam spot size equals to

11 mm, heated areas are not significantly overlapped with each other and yet the scans cover almost the entire tube length. Under scheme II, 20 pulses are sequentially applied with equal spacing in the axial direction. Here the beam width in the axial direction is 4 mm and again the pulses cover almost the entire tube length without significantly overlapped heating areas.

4.5.1 Wall Thickness Variation. The wall thickness variation along the circumference of tube that is bent under the optimal processing conditions for each scheme is shown in Fig. 18. Under schemes I and II, wall thickening occurs in the entire scanned range and wall thickness varies little in the unscanned range. No wall thinning at the extrados is very beneficial to bending tubes

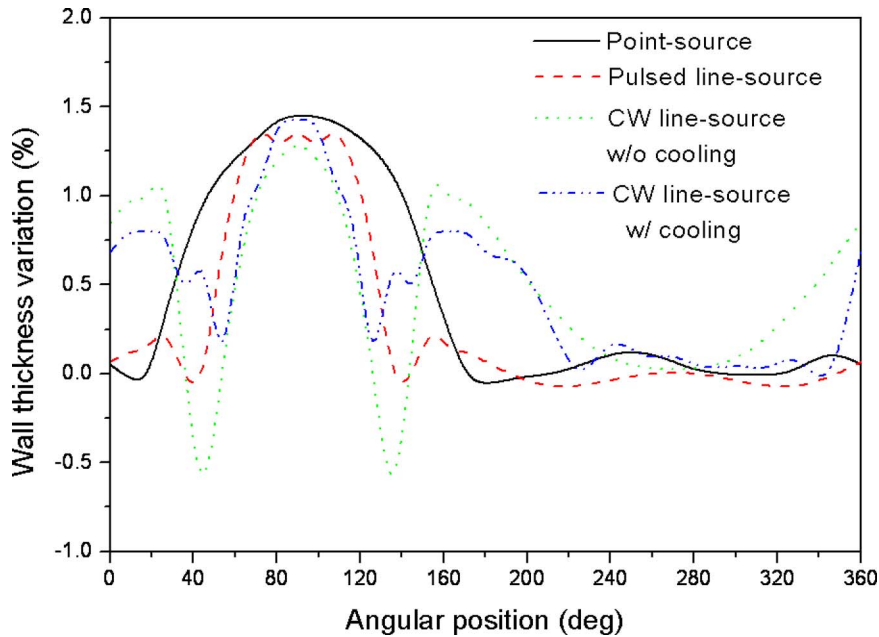


Fig. 18 Wall thickness variations under different scanning schemes [(a) scheme I, power=780 W, velocity=1.57 rad/s, beam diameter=11 mm; (b) Scheme II, power=425 W, irradiating time=1 s, beam width=4 mm; (c) Scheme III, power=1550 W, velocity=20 mm/s, beam width=4 mm; (d) Scheme IV, power=1550 W, velocity=20 mm/s, beam width=4 mm, cooling offset=50 mm]

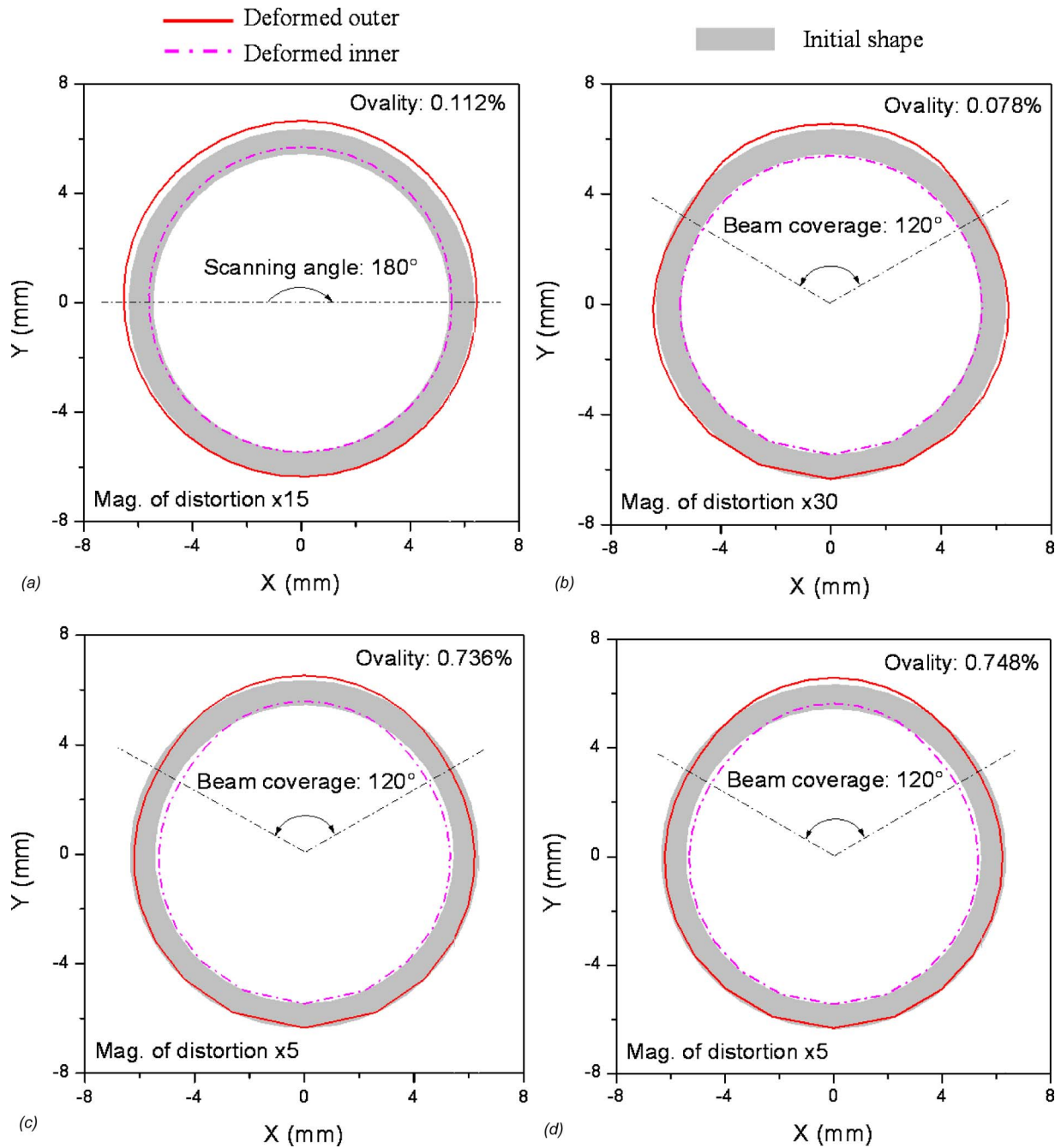


Fig. 19 Cross-section distortions under different scanning schemes [(a) Scheme I, power=780 W, velocity =1.57 rad/s, beam diameter=11 mm; (b) Scheme II, power=425 W, irradiating time=1 s, beam width=4 mm; (c) Scheme III, power=1550 W, velocity=20 mm/s, beam width=4 mm; (d) Scheme IV, power=1550 W, velocity=20 mm/s, beam width=4 mm, cooling offset=50 mm]

Table 3 Comparison of four scanning schemes. Tube length=100 mm. Scheme I: ($P=780$ W, $W=1.57$ rad/s, $d=11$ mm, eight equally-spaced sequential circumferential scans); Scheme II: ($P=425$ W, $t=1$ s, $w=4$ mm, 20 equally-spaced sequential pulses); Scheme III: ($P=1550$ W, $v=20$ mm/s, $w=4$ mm); and Scheme IV: ($P=1550$ W, $v=20$ mm/s, $w=4$ mm, cooling offset=50 mm). These conditions are optimal ones determined for each case.

Scheme	Bending angle (deg)	Bending radius (m)	Energy input (J)	Specific energy (J/deg)	Number of scanning	Time (s)	
						Scanning	Waiting
I	1.73	3.3	12480	7213.8	8	16	2100
II	2.22	2.58	8500	3828.8	20 (pulses)	20	2261
III	4.16	1.2	6781	1630	1	4.375	0
IV	5.83	0.86	6781	1163	1	4.375	0

with a small bending radius and to choosing tubes with thinner wall thickness to start with. The patterns of wall thickness variation under schemes III and IV are similar. Wall thickening is observed mainly at the scanned range and at the edge of the unscanned range as well, but the former is larger than the latter. This is believed to be due to the more prominent constraint in the circumferential direction under the schemes. Under scheme IV, the wall thickening fluctuates more due to more dramatic transitions from cooled and uncooled regions. Under scheme III, wall thinning occurs at the locations between two ranges of wall thickening because the material flows to the wall thickening range.

4.5.2 Cross-Section Distortion. Figure 19 shows the cross section of tube before and after laser bending under the same processing conditions for each scanning scheme as in Fig. 18. The cross-section distortion is quantitatively described by ovality which is defined as $(D_{\max} - D_{\min})/D$, where D_{\max} and D_{\min} are the maximum and minimum deformed outside diameters, respectively, and D is the outside diameter prior to deformation.

Under all schemes, the tube bulges out a bit in the heated area due to the tensile circumferential strain (e.g., Fig. 8) caused by the compressive axial strain. Under three schemes using a line laser source, the boundary between the heated and unheated materials (i.e., at both ends of the 120-deg beam coverage) bulges in a bit primarily due to the sudden change at the boundary. Under schemes III and IV, the cross-section distortion (0.736% and 0.748% in ovality, respectively) is larger than that under other two schemes (0.112% and 0.078% in ovality, respectively). This is primarily because the former represents a cumulative effect of the entire axial scan, while the latter mainly accounts for the effect of a single circumferential scan (as under scheme I) and a single pulse irradiation (as under scheme II) as subsequent scans or pulses are considered to be independent with each other.

4.5.3 Processing Efficiency. The processing efficiency under four scanning schemes is compared in Table 3. The specific energy is defined as the energy consumed to produce unit degree of bending angle. Clearly, scheme IV fares the best from the viewpoint of energy savings. Under schemes I and II, it is necessary to wait for the tube temperature to cool down to near the room temperature between two consecutive scans. Under schemes III and IV, the processing time only includes the actual scanning time. It is clear that the continuous line-source axial scanning offers an advantage compared to the continuous point-source circumferential scanning in both energy consumption and processing time.

5 Conclusions

The presented numerical model for laser tube bending is validated using existing experimental results under the first scanning scheme. Pulsed line-source axial procession can induce deformation in the tube depending on appropriate beam coverage. In line-source axial scanning, within a certain velocity range, higher ve-

locity can produce larger deformation. The application of water cooling is helpful to increase the bending deformation. The optimal cooling offset is related to the scanning velocity. The ovality in axial scanning is larger than that in circumferential scanning. The wall thickness variation is more intensive in axial scanning than that in circumferential scanning. Based on the numerical analysis, it is concluded that upsetting mechanism dominates in these three axial scanning schemes under the operating conditions presented. Line-source axial scanning is better than point-source circumferential scanning in both energy consumption and processing time. This paper focuses on a comparative study of four scanning schemes. Since the model under the first scheme was experimentally validated, it is expected to be reliable when it is applied in other schemes. The experimental study under these three schemes is beyond the scope of this paper.

Acknowledgment

The authors acknowledge the financial support from NIST under Grant No. ATP-00005269.

References

- [1] Silve, S., Steen, W. M., and Podschies, B., 1998, "Laser Forming Tubes: A Discussion of Principles," *Proceedings of ICALEO*, Sec. E, pp. 151–160.
- [2] Kraus, J., 1997, "Basic Process in Laser Bending of Extrusion Using the Upsetting Mechanism," *Laser Assisted Net Shape Engineering 2, Proceedings of the LANE'97*, Meisenbach Bamberg, Germany, Vol. 2, pp. 431–438.
- [3] Li, W., and Yao, Y. L., 2001, "Laser Bending of Tubes: Mechanism, Analysis and Prediction," *ASME J. Manuf. Sci. Eng.*, **123**, pp. 674–681.
- [4] Bachmann, F., 2002, "Present Technology, Industrial Applications and Future Prospects of High Power Diode Lasers," *ALT'01 International Conference on Advanced Laser Technologies*, Proc. SPIE, **4762**, pp. 1–5.
- [5] Lawrence, J., 2002, "A Comparative Investigation of the Efficacy of CO₂ and High-Power Diode Lasers for the Forming of EN3 Mild Steel Sheets," *Proc. Inst. Mech. Eng., Part A*, **216**, pp. 1481–1491.
- [6] Lopez, D., Dubsloff, J., Hofling, R., and Aswendt, P., 2003, "Application of a High-Power Diode Laser for Laser Bending," *Proc. Inst. Electr. Eng.*, **3097**, pp. 692–697.
- [7] Shealy, L. D., 2002, "Historical Perspective of Laser Beam Shaping," *Laser Beam Shaping III*, Proc. SPIE, **4770**, pp. 28–47.
- [8] Mucha, Z., Cabaj, M., Gradon, R., Pawlowski, M., and Widlaszewski, J., 2001, "Laser Forming of Plates by Use of Beam With Circular and Rectangular Cross Section," *Laser Assisted Net Shape Engineering, Proceedings of the LANE'2001*, Meisenbach Bamberg, Germany, Vol. 1, pp. 527–536.
- [9] Triantafyllidis, D., Li, L., and Stott, F. H., 2002, "The Effect of Beam Shape in Laser Surface Treatment of Ceramics," *Proceedings of ICALEO*, Sec. E.
- [10] Churchill, S. W., and Berstein, M., 1977, "A Correlating Equation for Forced Convection From Gases and Liquids to a Circular Cylinder in Crossflow," *ASME J. Heat Transfer*, **99**, pp. 300–306.
- [11] Kobayashi, S., 1989, *Metal Forming and the Finite Element Method*, Oxford University Press, New York.
- [12] Boley, B. A., and Weiner, J. H., 1997, *Theory of Thermal Stresses*, Dover, New York.
- [13] Vollertsen, F., 1994, "Mechanism and Models for Laser Forming," *Laser Assisted Net Shape Engineering, Proceedings of the LANE'94*, Meisenbach Bamberg, Germany, Vol. 1, pp. 345–360.
- [14] Myers, R. H., and Montgomery, D. C., 1995, *Response Surface Methodology*, Wiley, New York.
- [15] Li, W., and Yao, Y. L., 2001, "Laser Forming With Constant Line Energy," *Int. J. Adv. Manuf. Technol.*, **17**, pp. 196–203.